Local and average structure of Mn- and La-substituted $BiFeO_3$

Bo Jiang and Sverre M. Selbach*

Department of Materials Science and Engineering,
NTNU Norwegian University of Science and Technology, 7491 Trondheim, Norway

*Correspondence should be addressed to selbach@ntnu.no

The local and average structure of solid solutions of the multiferroic perovskite $BiFeO_3$ is investigated by synchrotron X-ray diffraction (XRD) and electron density functional theory (DFT) calculations. The average experimental structure is determined by Rietveld refinement and the local structure by total scattering data analyzed in real space with the pair distribution function (PDF) method. With equal concentrations of La on the Bi site or Mn on the Fe site, La causes larger structural distortions than Mn. Structural models based on DFT relaxed geometry give an improved fit to experimental PDFs compared to models constrained by the space group symmetry. Berry phase calculations predict a higher ferroelectric polarization than the experimental literature values, reflecting that structural disorder is not captured in either average structure space group models or DFT calculations with artificial long range order imposed by periodic boundary conditions. Only by including point defects in a supercell, here Bi vacancies, can DFT calculations reproduce the literature results on the structure and ferroelectric polarization of Mn-substituted $BiFeO_3$. The combination of local and average structure sensitive experimental methods with DFT calculations is useful for illuminating the structure-property-composition relationships in complex functional oxides with local structural distortions.

Introduction

Lead-free piezoelectrics are environmentally friendly alternatives to the state-of-the-art lead-containing $Pb(Zr,Ti)O_3$ (PZT) based materials [1]. $BiFeO_3$ is the most studied multiferroic material and crystallizes in a rhombohedral polar *R*3*c* structure [2-5], displays high Néel (T_N) and Curie (T_C) temperatures of 370°C and 830°C, respectively, and a large spontaneous

polarization (*Ps*) of ~90μC/cm^2 [6-10]. Solid solutions based on $BiFeO_3$ have shown promising piezoelectric properties around morphotropic phase boundaries (MPB), and substitution on the *A* and *B* site of $BiFeO_3$ has been the topic of numerous studies [11-14]. Substituting Fe with Mn [15-19], and Bi with La [20-24], are the most common isovalent B-site and A-site modifications of $BiFeO_3$, respectively. The majority of doping studies have focused on thin films or the macroscopic properties and average structure of ceramics. However, the effect of local symmetry breaking around dopant atoms, and the structural coherence, has received little attention. As local structural distortions affect the chemical bonding, such distortions are imperative to the structure-property relationships.

La doping of $BiFeO_3$ ceramics has been reported to enhance the macroscopic ferroelectric properties [25], although this implies a dilution of the Bi sublattice. This is surprising as the Bi $6s^2$ lone pair is primarily responsible for ferroelectricity. Improved ferroelectric properties of La-substituted $BiFeO_3$ ceramics may thus stem from suppression of the secondary phases mullite, $Bi_2Fe_4O_9$, and sillenite, $Bi_{25}FeO_{39}$, which are difficult to avoid [26]. $Bi_{1-x}La_xFeO_3$ shows complete solid solubility for all values of x, but the phase diagram is complex, with experimental findings of compositional regions with more than two coexisting phases, which in principle violates Gibbs phase rule [22]. $BiFe_{1-x}Mn_xO_3$ does not show full solid solubility at ambient pressure, and decomposes to mullite and sillenite phases for $x > 0.3$ [17]. High pressure synthesis, on the other hand, allows complete solid solubility of $BiMnO_3$ and $BiFeO_3$ [27, 28]. Manganese substituted $BiFeO_3$ is prone to oxygen hyperstoichiometry ($3+\delta$), which strongly affect the crystal lattice, electrical conductivity, and phase-transition temperatures [16, 17]. The *R*3*c* phase field for $BiFe_{1-x}Mn_xO_{3+\delta}$ extends up to $x_{Mn} \leq 0.3$ and up to $x_{La} = 0.1$ for $Bi_{1-x}La_xFeO_3$, implying that the ferroelectric *R*3*c* structure is more sensitive to dilution of the Bi sublattice than the Fe sublattice. A summary of literature data on Mn and La substitution of $BiFeO_3$ is provided in Table 1.

In this work we use pair distribution functions (PDF) obtained from high energy synchrotron X-ray diffraction to investigate the local and average structure of La and Mn-substituted $BiFeO_3$. Due to the difference in X-ray scattering lengths between light oxygen and the heavier cations in $BiFeO_3$, oxygen positions can only be extracted with limited accuracy, while the method is highly sensitive to structural disorder in the cation sublattices. We find that the same dopant concentration causes greater local distortions when introduced to the Bi sublattice than the Fe sublattice. Our Density functional theory (DFT) calculations show that the average structure models from conventional reciprocal space diffraction give higher

calculated spontaneous polarizations than the experimentally reported values. Attention to local structural distortions, and including point defects, in the DFT model is required to reproduce the experimental structure and spontaneous polarization of Mn-substituted $BiFeO_3$.

Table 1. Selected properties of Mn and La substitution of $BiFeO_3$

	$BiFeO_3$	$Bi_{1-x}La_xFeO_3$	$Bi_{1-x}Mn_xFeO_3$
Magnetic moment Fe/Mn (μ_B)	3.7±0.03[15]	3.79±0.03, x=0.07 [15]	3.35, x=0.1 [24] 2.98, x=0.2 [24]
Spontaneous polarization ($\mu C/cm^2$)	90-100, DFT [7] 50-60, film [5]	42, x=0.2 [29] 22, x=0.3 [30]	10, x=0.3 [15]
Curie temperature (℃)	830 [9, 10]	754, x=0.05 [20] 677, x=0.1 [20, 23]	773, x=0.1 [17] 715, x=0.2 [17] 660, x=0.3 [17]

2. Experimental and computational details

Samples of $BiFeO_3$ (BFO), $BiFe_{0.875}Mn_{0.125}O_3$ (BFMO125), $BiFe_{0.75}Mn_{0.25}O_3$ (BFMO25) and $Bi_{0.9}La_{0.1}FeO_3$ (BLFO10) were prepared by a conventional solid-state synthesis route described previously [16, 17, 23], where the samples are fired in air for 5 min at 900 °C and furnace cooled at a rate of ~200 °C/hour. X-ray total scattering data were collected at beamline 11-ID-B (90 keV with λ=0.13702Å) at Argonne National Lab. The pair distribution function (PDF) was obtained with the PDFgetX3 software [31] using a Q_{max} of 23.0 $Å^{-1}$. Structural modeling with full range fitting of the G(r) function was carried out using the PDFgui software [32] with the parameters obtained from the XRD Rietveld refinements as starting structural models. The crystal structure was analyzed by Rietveld refinement using the General Structure Analysis System (GSAS) program [33].

Density functional theory (DFT) calculations were performed with the Vienna Ab initio Simulation Package (VASP) [34, 35] using the PBEsol functional [36]. The standard PBE PAW potentials Bi_d ($5d^{10}6s^26p^3$), La ($5s^25p^65d^16s^2$), Fe_pv ($3p^63d^74s^1$), Mn_sv($3s^23p^64s^23d^5$) and O ($2s^2p^4$) supplied with VASP were used and plane waves were expanded up to a cutoff energy

of 550 eV. Brillouin zone integration was done on a 4×4×2 gamma centred k-point grid for the hexagonal $Bi_6Fe_6O_{18}$ cell with 30 atoms, with corresponding k-point densities for larger cell sizes. The Hellman-Feynman forces on the atoms were relaxed until they were below 10^{-3} eV/Å. The magnetic order of the Fe sublattice was initialized as the G-type collinear antiferromagnetic ordering in concordance with the magnetic order of bulk BFO [19]. Hubbard U values of 4, 3 and 10 eV were applied to Fe 3d, Mn 3d and La 4f, respectively. Bader charges were calculated as described in ref. [37], and ferroelectric polarization was calculated by the Berry phase approach [38].

3. Results and discussion

Phase pure $BiFeO_3$ (BFO) $BiFe_{0.875}Mn_{0.125}O_3$ (BFMO125), $BiFe_{0.75}Mn_{0.25}O_3$ (BFMO25) and $Bi_{0.9}La_{0.1}FeO_3$ (BLFO10) bulk powders were successfully prepared by solid state synthesis and the synchrotron XRD patterns shown in Fig. 1a. All patterns could be indexed with the *R*3*c* trigonal space group in agreement with previous work [17, 23], and the refined average structural parameters are summarized in Table 2. The *R*3*c* structure with hexagonal axis is shown in Fig. 1b. We adopted the atomic positions setting used by Sosnowska et al. [19] with the Bi fixed at the origin, Fe in (0,0,z) and O in (x,y,z).

In order to simulate the experimental composition of $BiFe_{0.875}Mn_{0.125}O_3$ and $BiFe_{0.75}Mn_{0.25}O_3$, 30 atoms hexagonal unit cell with compositions $Bi_6Fe_5MnO_{18}$ and $Bi_6Fe_4Mn_2O_{18}$ were used. For $Bi_{0.9}La_{0.1}FeO_3$ the composition $Bi_5LaFe_6O_{18}$ was used as an approximation, and a $Bi_4La_2Fe_6O_{18}$ cell was included to examine the trend upon extrapolation. The DFT simulations reproduced the experimental structural trends with chemical composition, as shown in Fig. 2. The systematic subtle underestimation of the lattice parameters is a common anomaly of DFT calculations with the PBEsol functional, which still reproduces experimental volumes more accurately than e.g. LDA or PBE-GGA [36].

Table 2. Rietveld refinement results at room temperature of $BiFeO_3$ (BFO), $BiFe_{0.875}Mn_{0.125}O_3$ (BFMO125) $BiFe_{0.75}Mn_{0.25}O_3$ (BFMO25) and $Bi_{0.9}La_{0.1}FeO_3$ (BLFO10) with *R*3*c* hexagonal space group.

	BFO	BFMO125	BFMO25	BLFO10
a(Å)	5.581(4)	5.580(6)	5.574(8)	5.579(9)
c(Å)	13.879(3)	13.867(5	13.831(4)	13.813(8)
z(Fe/Mn)	0.221(4)	0.223(1)	0.224(8)	0.226(9)
x(O)	0.442(5)	0.443(6)	0.441(7)	0.435(8)
y(O)	0.008(5)	0.010(9)	0.007(8)	0.000(0)
z(O)	0.956(0)	0.954(2)	0.955(9)	0.959(0)
R_w(%)	3.29	2.73	3.27	3.70
Volume(Å^3)	374.43	374.00	372.26	372.48

A simple, empirical relationship between ferroelectric Curie temperature T_c and spontaneous polarization P_s in displacive ferroelectric perovskites was reported by Abrahams et al. [39]: $T_c = (\kappa/2k_B)(\Delta z)^2$ where κ is a force constant, k_B is the Boltzmann's constant, $\Delta z = [0.25\text{-}z(\text{Fe})]\times c_{hex}$ Å is the polar displacement of Fe/Mn along the *c* axis in hexagonal *R*3*c* BFO, and $P_s = (258\pm9)\Delta z$ μC/cm^2. The T_c decreases as the *z*(Fe) increases towards the centrosymmetric position of z = 0.25 on the right hand side of the Fig. 3, in agreement with previous work [17]. The empirical relationship of Abrahams predicts a spontaneous polarization of P_s =102.4±3.6 μC/cm^2 for BFO which is very close to DFT calculated values [7]. The most striking deviation between the experimental and computational results in Fig. 3 is found for the displacement of Fe(Mn). A possible source of this discrepancy is that in a 30 atom cell with more than one cation on the same sublattice, the periodic boundary conditions in DFT calculations induce an artificial long range order of the dopant atoms La and Mn. To investigate the possibility of structural disorder not easily captured by periodic boundary conditions DFT, we use pair distribution functions (PDF) from high energy synchrotron total scattering. The PDFs of pure and La/Mn-substituted BFO could be fitted to a simple *R*3*c* structural model as shown in Fig. 4a, where the high r region probes the intermediate and average structure, while the low r region shows the local structure. It should be noted that in the Fig. 4(b), the Fe/Mn position from PDF average range and Rietveld analysis data show good agreement in trend, but with a systematic shift between the two different analysis methods.

The isotropic atomic thermal displacement factors from PDF refinement over a 30 Å range increase with increasing concentration of Mn, and this as a clear signature of enhanced structural disorder. The fitted PDFs for each sample composition was decomposed into partial PDFs showing only specific atom pairs, as depicted in Fig. 5a together with the experimental PDFs. PDF peaks in the local (b-c) and intermediate (d-e) structure range are shown in Fig. 5b-d. With both Mn and La doping the PDF peaks become more smeared than for pure BFO, reflecting local structural disorder and a distribution of bond lengths. The difference between the PDF peaks of pure and doped BFO does not significantly vary between local structure and intermediate range structure, showing that doping affects both the local symmetry of the lattice as well as the long range structural coherence. Doping causes a similar smearing of both the Bi-Bi and the Bi-Fe PDF peaks, see Figure 5(a-e), regardless of whether the chemical substitution takes place on the Bi or Fe sublattice. The ferroelectric displacements in the cation sublattices of BFO are hence strongly coupled as both cations are displaced towards the faces of the oxygen octahedra, with no oxygen anions directly between to shield the electrostatic repulsion between the cations [40]. In the zoomed-in regions in Fig. 5 (b-e) it is evident that the perturbation of the PDF caused by 10% La on the Bi site is stronger than for 25% Mn on the Fe site. This difference probably stems from the importance of the $6s^2$ lone pair of Bi^{3+} for stabilizing the ferroelectric *R*3*c* structure; La^{3+} without a lone pair causes greater structural distortions than Mn^{3+} which is similar in size to Fe^{3+}, albeit a Jahn-Teller active d^4 high spin cation. A more detailed discussion of the role of manganese oxidation state is given further below.

Closer inspection of the relaxed structures from DFT calculations reveal strong local distortions around the dopant atoms. Mn octahedra display a volume of 10.59 $Å^3$ compared to 10.84 $Å^3$ for Fe octahedra in undoped $BiFeO_3$. Simultaneously, Mn doping causes a reduction of 0.24 and 0.46% of the Bi dodecahedral volume for $Bi_6Fe_5MnO_{18}$ and $Bi_6Fe_4Mn_2O_{18}$, respectively. In $Bi_5LaFe_6O_{18}$ the La dodecahedron is, surprisingly, only 0.07 $Å^3$ smaller than the Bi dodecahedron. La doping also causes a 0.43% reduction of the Fe octahedral volumes, and the complex interplay between dopants and perturbations between the two cation sublattices can not be attributed to one single effect. We take into account the sum of all these perturbations by simulating PDFs from the DFT calculated structures (Fig. 5 (f-i). These simulated PDFs better reproduce the experimental PDFs (Fig. 5 (b-e)), including the differences between undoped and doped BFO, than the fitted PDFs in Fig. 4. The reason is that small-box fitting with an *R*3*c* model in PDFgui inherently presumes long range structural

coherence, while the DFT calculated structural model allows local symmetry-breaking displacements. Another kind of direct comparisons between the PDFs from experimental and PDFs form DFT calculated structures are shown in Fig. 4S in supplementary file.

A zoom in on the low r range PDF in Fig. 6 highlights how La^{3+} causes structural disorder in BFO. Flattening of the triple peak from 3.02 to 3.59 Å, which corresponds to Bi-Fe distances, as well as a lower intensity of the Bi-Bi peaks, shows that La causes a broader distribution of bond lengths on the local scale. To illustrate the structural disorder caused by La^{3+}, we also compare the low-r range PDF of Mn-doped $BiFe_{0.875}Mn_{0.125}O_3$ with $Bi_{0.9}La_{0.1}FeO_3$ as shown in Fig. 7. Note that the partial PDFs of Bi-Fe bond peak obtained more disorder after La doping than Mn doping, even though both La or Mn has little contribution to the A-B bond peaks. This can be understood as a perturbation of the ferroelectric order and the microscopic origin of both the reduction in Curie temperature with La substitution as well as an enhancement of the piezoelectric coefficient [41-43]. The latter effect could stem from both an enhancement of domain wall mobility at a mesoscopic length scale, or a flattening of the polarization direction energy landscape on the unit cell scale.

The local structural disorder caused by doping, evident from the PDFs in Fig. 5 and 6, is not easily captured by conventional reciprocal space diffraction. The multiferroic properties are strongly correlated with local structure and the chemical bonds, e.g. antiferromagnetism arising from Fe-O-Fe superexchange and ferroelectricity from partial covalency between Bi and O. We thus expect structural disorder to affect the functional properties. To investigate the intrinsic ferroelectric properties in more detail we calculated the total energy for displacement of ions from the centrosymmetric positions (0% distortion) to the equilibrium non-centrosymmetric positions (-100% and 100% distortion), as plotted in Fig. 8. Pure BFO gives a symmetric double-well which is typical for displacive ferroelectrics, and the minima correspond to the fully relaxed polar *R*3*c* structure with opposite directions of polarization. The spontaneous polarizations P_S calculated by the Berry phase method, see Table 3, is in agreement with previous theoretical investigations [7]. After introducing dopants it can be seen from Fig. 8 that Mn on the Fe site does not lift the symmetry of the double-well for $x_{Mn} = 1/6$, and only a subtle asymmetry is observed for $x_{Mn} = 1/3$. A low content of Mn in BFO hence has little impact on the symmetry of the structure and does not alter the space group. This is also reflected by the almost negligible reduction of the calculated P_S (Table 3) in Mn-substituted BFO. This result is however surprising given the strong reduction of ferroelectric T_C and polar

distortion of the unit cell upon Mn doping found experimentally[16, 17], and this is discussed further below.

Table 3. Volume, polarization (P_s), atomic magnetic moments (μ_B) and average Bader charges for Mn and La substituted BFO from PBEsol+U calculations.

x /element	a (Å)	c (Å)	P_s	Mag	Bader Charge	
			(μC/cm^2)	(Fe/Mn)	Bi(La)	Fe(Mn)
$Bi_6Fe_6O_{18}$	5.553	13.759	97	4.1/-	1.85(-)	1.74(-)
$Bi_6Fe_5MnO_{18}$	5.552	13.740	96	4.1/3.6	1.85(-)	1.74(1.73)
$Bi_6Fe_4Mn_2O_{18}$	5.551	13.718	92	4.1/3.6	1.85(-)	1.73(1.73
$Bi_5LaFe_6O_{18}$	5.557	13.691	82	4.1/-	1.85(2.15)	1.74(-)
$Bi_4La_2Fe_6O_{18}$	5.562	13.610	67	4.1/-	1.85(2.14)	1.74(-)
$Bi_{23}Fe_{21}Mn_3O_{72}$	11.049 (5.525)	13.664	25	4.1/3.0	1.86(-)	1.75(1.88)

La-substitution of Bi has a much stronger effect on the ferroelectric double-well than Mn, in line with the experimental PDFs in Fig. 5. La causes more smearing of the PDF peaks than comparable amounts of Mn, implying greater structural disorder and a concomitantly more flat energy landscape for displacements of cations, consistent with a more shallow ferroelectric double-well. This corresponds to the lower ferroelectric polarization calculated for La-substituted $BiFeO_3$ in Table 3. The depth of the ferroelectric wells relative to the centrosymmetric reference structure decreases more with La than a corresponding concentration of Mn. We note 1/6 and 1/3 La in *R*3*c* BFO is an artificial extrapolation as both paraelectric *Pnma* and antiferroelectric *Pbam* are found experimentally for these nominal compositions [22, 43]. We also note that macroscopic ferroelectric properties of a ceramic polycrystal also depends strongly on the microstructure of the grains and domain structure within the grains.[44-46] This length scale and level of complexity is not easily modelled by conventional DFT calculations.

The physical parameters obtained from the DFT calculations are summarized in Table 3. It is well established that Mn-doping does not alter the space group of $BiFe_{1-x}Mn_xO_3$ for $x \leq 0.3$, in line with the XRD and PDF results above. However, experiments show that the ferroelectric T_C and polar unit cell distortion is strongly reduced with Mn content [16, 17], and this is not

reproduced in the DFT calculations of stoichiometric cell as Mn substitution had little influence on the spontaneous polarization P_S and unit cell volume (Table 3). The partial density of states (PDOS) of stoichiometric $Bi_6Fe_5MnO_{18}$ shown in Fig. 9 (a) reveals that Mn^{3+} gives rise to a state in the middle of the band gap, and this can be assigned to the single e_g *d*-electron of high spin d^4 Mn^{3+}. This implies that Mn^{3+} gives a lower bandgap, as reported for thin films grown by pulsed laser deposition (PLD), which is typically done in low pO_2 compared to ceramic processing [18]. However, excess oxygen compensated by cation vacancies and partial oxidation of Mn^{3+} to Mn^{4+} has previously been shown to strongly affect the properties of $BiFe_{1-x}Mn_xO_{3+\delta}$ [16, 17]. Oxidation of $BiFe_{1-x}Mn_xO_3$ can be described by the following Kröger-Vink equation:

$$\delta/2\,O_2 + 2\delta Mn_{Fe}^{x} \leftrightarrow 2\delta Mn_{Fe}^{\bullet} + \delta/3\,V_{Bi}^{'''} + \delta/3\,V_{Fe}^{'''} \qquad (1)$$

Here $Mn^{\bullet}$ corresponds to Mn^{4+} on a Fe^{3+} site, hence the relative charge of +1. Mn^{4+} is a d^3 cation without the e_g electron found in the band gap in the PDOS in Fig. 9a. One obvious reason for the discrepancy between the DFT calculations summarized in Table 3 and the experimental structure is thus that Mn-substituted bulk BFO prepared in air atmosphere may be inherently oxygen rich with charge compensation by Mn^{4+} and site compensation by cation vacancies. This possibility is further supported by recent EELS investigations of Mn-doped thin films [47].

However, as excess oxygen can be avoided by annealing in inert atmosphere [16, 17], we also address the possibility of Bi deficiency charge compensated by oxidation of Mn. Inert atmosphere, e.g. N_2, has been shown to destabilize the perovskite BFO towards peritectic decomposition and promote evaporation of Bi [9, 26]. To test this hypothesis we constructed a $Bi_{23}Fe_{21}Mn_3O_{72}$ model corresponding to a 2x2x1 hexagonal supercell with one Bi vacancy and three Mn on Fe sites. This can formally be expressed by the following defect reaction:

$$Bi_{Bi}^{x} + 3Mn_{Fe}^{x} \leftrightarrow Bi(g) + V_{Bi}^{'''} + 3Mn_{Fe}^{\bullet} \qquad (2)$$

Here the bismuth vacancy with relative charge -3 is charge compensated by the oxidation of three Mn. The calculated total and partial DOS of $Bi_6Fe_5MnO_{18}$ and $Bi_{23}Fe_{21}Mn_3O_{72}$ are compared in Fig. 9 (b). The oxidation of three Mn^{3+} to Mn^{4+}, as highlighted by the calculated Bader charges in Table 3, removes the gap state found in stoichiometric $Bi_6Fe_5MnO_{18}$ as these states become unoccupied and are lifted into the conduction band. The calculated polarization

P_s decreases significantly, to 25 μC/cm^2, upon introduction of a Bi vacancy. The relaxed lattice parameters, especially the polar c-axis, contracts in concordance with experiments presented here and in the literature [17, 27]. Supercell modeling of Mn-doped BFO with a bismuth vacancy thus reproduces the experimentally observed structure and properties much better than models with only Mn for Fe substitution. Bismuth vacancies have also recently been shown to control the domain wall conductivity of BFO [44], further emphasizing the need for taking point defects and local structural distortions into account to establish structure-property relationships.

4. Conclusions

In summary, the local and average structure of La- and Mn-substituted $BiFeO_3$ was investigated by DFT calculations and PDF and Rietveld analysis of synchrotron X-ray total scattering data. La doping was found to induce stronger local structural disorder than equivalent amounts of Mn doping, and DFT calculations showed that the local symmetry breaking caused by La on the Bi site is more pronounced than for Mn on the Fe site. Structural models inferred from DFT relaxed structures gave better fits to the experimental PDFs than models based on the space group *R*3*c* where the ions are confined to atomic positions obeying the space group symmetry. In order to reproduce experimental trends in lattice parameters with Mn doping, the possibility that Bi vacancies can give rise to charge compensating oxidation of Mn was supported by DFT calculations. We demonstrate that the combination of PDF and DFT to study inherent local symmetry breaking caused by doping can provide a deeper microscopic understanding of complex solid solutions.

Acknowledgements

We thank J. A. Kurzman, S. A. Corr and R. Seshadri for performing the synchrotron measurements. J. Glaum is acknowledged for discussions. This work was supported by the Research Council of Norway through the SYNKNØYT project 228571/F50 “Local structure of lead-free relaxor piezoelectrics (LOCPIEZO)”. Computational resources were provided by the Norwegian Metacenter for Computational Science (NOTUR) through the project NN9264K.

REFERENCES

[1] J. Rödel, W. Jo, K.T.P. Seifert, E.M. Anton, T. Granzow, D. Damjanovic, J .Am. Ceram. Soc. 92(6) (2009) 1153-1177.

[2] G. Catalan, J.F. Scott, Adv. Mater. 21(24) (2009) 2463-2485.

[3] F. Kubel, H. Schmid, Acta Crystallogr. B46 (1990) 698-702.

[4] T. Rojac, A. Bencan, B. Malic, G. Tutuncu, J.L. Jones, J.E. Daniels, D. Damjanovic, J. Am. Ceram. Soc. 97(7) (2014) 1993.

[5] J. Wang, J.B. Neaton, H. Zheng, V. Nagarajan, S.B. Ogale, B. Liu, D. Viehland, V. Vaithyanathan, D.G. Schlom, U.V. Waghmare, N.A. Spaldin, K.M. Rabe, M. Wuttig, R. Ramesh, Science 299(5613) (2003) 1719-22.

[6] D. Lebeugle, D. Colson, A. Forget, M. Viret, Appl. Phys. Lett. 91(2) (2007) 022907.

[7] J.B. Neaton, C. Ederer, U.V. Waghmare, N.A. Spaldin, K.M. Rabe, Phys. Rev. B 71(1) (2005) 014113.

[8] S.M. Selbach, T. Tybell, M.A. Einarsrud, T. Grande, Adv. Mater. 20(19) (2008) 3692.

[9] S.M. Selbach, T. Tybell, M.A. Einarsrud, T. Grande, J. Solid State Chem. 183(5) (2010) 1205-1208.

[10] D.C. Arnold, K.S. Knight, F.D. Morrison, P. Lightfoot, Phys. Rev. Lett. 102 (2009) 027602.

[11] S. Fujino, M. Murakami, V. Anbusathaiah, S.H. Lim, V. Nagarajan, C.J. Fennie, M. Wuttig, L. Salamanca-Riba, I. Takeuchi, Appl. Phys. Lett. 92(20) (2008) 202904.

[12] D. Kan, L. Palova, V. Anbusathaiah, C.J. Cheng, S. Fujino, V. Nagarajan, K.M. Rabe, I. Takeuchi, Adv. Funct. Mater. 20(7) (2010) 1108.

[13] M.I. Morozov, M.A. Einarsrud, T. Grande, Appl. Phys. Lett. 101(25) (2012) 252904.

[14] X.D. Qi, J. Dho, R. Tomov, M.G. Blamire, J.L. MacManus-Driscoll, Appl. Phys. Lett. 86(6) (2005) 062903.

[15] M. Kumar, K.L. Yadav, Appl. Phys. Lett. 91(24) (2007) 242901.

[16] S.M. Selbach, T. Tybell, M.A. Einarsrud, T. Grande, Phys. Rev. B 79(21) (2009) 214113.

[17] S.M. Selbach, T. Tybell, M.A. Einarsrud, T. Grande, Chem. Mater. 21(21) (2009) 5176-5186.

[18] X.S. Xu, J.F. Ihlefeld, J.H. Lee, O.K. Ezekoye, E. Vlahos, R. Ramesh, V. Gopalan, X.Q. Pan, D.G. Schlom, J.L. Musfeldt, Appl. Phys. Lett. 96(19) (2010) 192901.

[19] I. Sosnowska, W. Schaffer, W. Kockelmann, K.H. Andersen, I.O. Troyanchuk, Appl. Phys. A Mater. Sci. Proc. 74 (2002) S1040-S1042.

[20] S. Karimi, I.M. Reaney, Y. Han, J. Pokorny, I. Sterianou, J. Mater. Sci. 44(19) (2009) 5102-5112.

[21] Y.H. Lee, J.M. Wu, C.H. Lai, Appl. Phys. Lett. 88(4) (2006) 042903.

[22] D.A. Rusakov, A.M. Abakumov, K. Yamaura, A.A. Belik, G. Van Tendeloo, E. Takayama-Muromachi, Chem. Mater. 23(2) (2011) 285-292.

[23] R. Saeterli, S.M. Selbach, P. Ravindran, T. Grande, R. Holmestad, Phys. Rev. B 82(6) (2010) 064102.

[24] I. Sosnowska, W. Schafer, W. Kockelmann, I.O. Troyanchuk, Mater. Sci. Forum 378 (2001) 616-620.

[25] Z.X. Cheng, A.H. Li, X.L. Wang, S.X. Dou, K. Ozawa, H. Kimura, S.J. Zhang, T.R. Shrout, J. Appl. Phys. 103(7) (2008) 07E507.

[26] S.M. Selbach, M.-A. Einarsrud, T. Grande, Chem. Mater. 21(1) (2009) 169-173.

[27] M. Azuma, H. Kanda, A.A. Belik, Y. Shimakawa, M. Takano, J. Magn. Magn. Mater. 310(2) (2007) 1177-1179.

[28] A.A. Belik, A.M. Abakumov, A.A. Tsirlin, J. Hadermann, J. Kim, G. Van Tendeloo, E. Takayama-Muromachi, Chem. Mater. 23(20) (2011) 4505-4514.

[29] S.R. Das, P. Bhattacharya, R.N.P. Choudhary, R.S. Katiyar, J. Appl. Phys. 99(6) (2006) 066107.

[30] S.T. Zhang, L.H. Pang, Y. Zhang, M.H. Lu, Y.F. Chen, J. Appl. Phys. 100(11) (2006) 114108.

[31] P. Juhas, T. Davis, C.L. Farrow, S.J.L. Billinge, J. Appl. Crystallogr. 46 (2013) 560-566.

[32] C.L. Farrow, P. Juhas, J.W. Liu, D. Bryndin, E.S. Bozin, J. Bloch, T. Proffen, S.J.L. Billinge, J. Phys.: Condens. Matter 19(33) (2007) 335219.

[33] A.C. Larson, R.B. von Dreele, General Structure Analysis System (GSAS) (University of Califonia, USA, 2001).

[34] G. Kresse, J. Furthmuller, Phys. Rev. B 54(16) (1996) 11169-11186.

[35] G. Kresse, D. Joubert, Phys. Rev. B 59(3) (1999) 1758-1775.

[36] J.P. Perdew, A. Ruzsinszky, G.I. Csonka, O.A. Vydrov, G.E. Scuseria, L.A. Constantin, X.L. Zhou, K. Burke, Phys. Rev. Lett. 100(13) (2008) 136406.

[37] W. Tang, E. Sanville, G. Henkelman, J. Phys.: Condens. Matter 21(8) (2009) 084204.

[38] N.A. Spaldin, J. Solid State Chem. 195 (2012) 2-10.

[39] S.C. Abrahams, S.K. Kurtz, P.B. Jamieson, Phys. Rev. 172(2) (1968) 551.

[40] N.W. Thomas, A. Beitollahi, Acta Crystallogr. B 50 (1994) 549-560.

[41] I.O. Troyanchuk, D.V. Karpinsky, M.V. Bushinsky, O.S. Mantytskaya, N.V. Tereshko, V.N. Shut, J. Am. Ceram. Soc. 94(12) (2011) 4502-4506.

[42] I.O. Troyanchuk, D.V. Karpinsky, M.V. Bushinsky, V.A. Khomchenko, G.N. Kakazei, J.P. Araujo, M. Tovar, V. Sikolenko, V. Efimov, A.L. Kholkin, Phys. Rev. B 83(5) (2011) 054109.

[43] D.V. Karpinsky, I.O. Troyanchuk, M. Tovar, V. Sikolenko, V. Efimov, A.L. Kholkin, J. Alloys Comp. 555 (2013) 101-107.

[44] T. Rojac, A. Bencan, G. Drazic, N. Sakamoto, H. Ursic, B. Jancar, G. Tavcar, M. Makarovic, J. Walker, B. Malic, D. Damjanovic, Nature Materials 16 (2016) 322-327.

[45] S. Karimi, I.M. Reaney, Y. Han, J. Pokorny, I. Sterianou, J. Mater. Sci. 44(19) (2009) 5102-5112.

[46] F. Yan, T.J. Zhu, M.O. Lai, L. Lu, Scripta Mater 63(7) (2010) 780-783.

[47] I. MacLaren, B. Sala, S.M.L. Andersson, T.J. Pennycook, J. Xiong, Q.X. Jia, E.M. Choi, J.L. MacManus-Driscoll, Nanoscale Res. Lett. 10 (2015) 407.

FIGURES

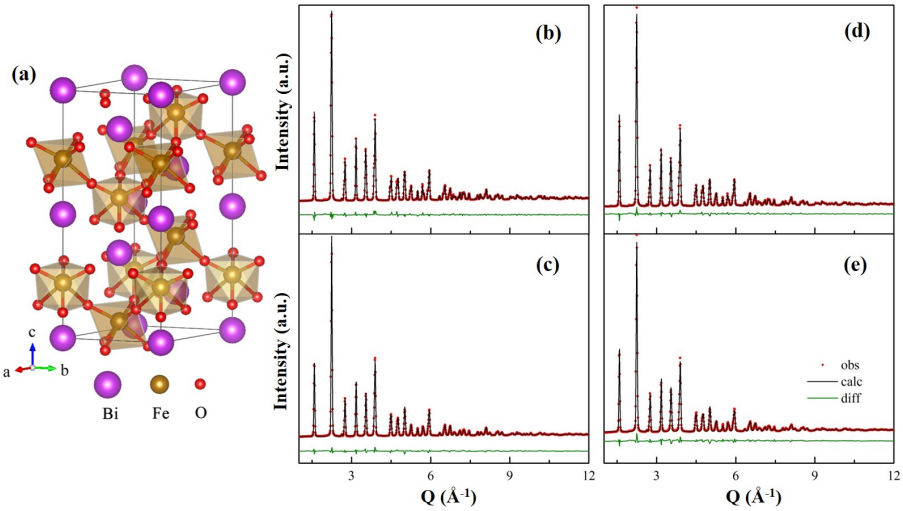

Fig. 1. (a) The hexagonal *R*3*c* $BiFeO_3$ unit cell with 30 atoms. (b)-(e) Rietveld pattern for *R*3*c* $BiFeO_3$ (BFO), $BiFe_{0.875}Mn_{0.125}O_3$ (BFMO125), $BiFe_{0.75}Mn_{0.25}O_3$ (BFMO25) and $Bi_{0.9}La_{0.1}FeO_3$ (BLFO10) showing the experimental (red crosses), calculated (black line) and difference (green line) powder XRD profiles.

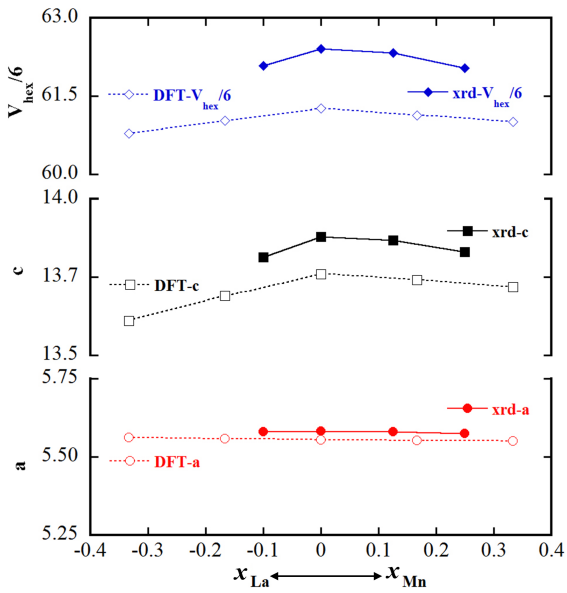

Fig. 2. DFT calculated (open symbols with dashed lines) and experimental (filled symbols with solid lines) structure parameters of *c*, *a* and $V_{hex}/6$ as a function of chemical composition ($Bi_{1-x}La_xFeO_3$ and $BiFe_{1-x}Mn_xO_3$).

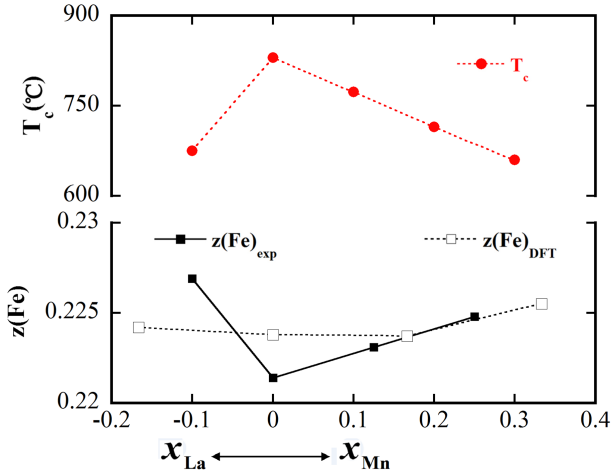

Fig. 3. The DFT calculated (open symbols with dashed lines) and experiment (filled symbols with solid lines) of polar cation relative displacements as a function of chemical composition ($Bi_{1-x}La_xFeO_3$ and $BiFe_{1-x}Mn_xO_3$). The ferroelectric Curie temperatures with different chemical compositions also are plotted [17, 23].

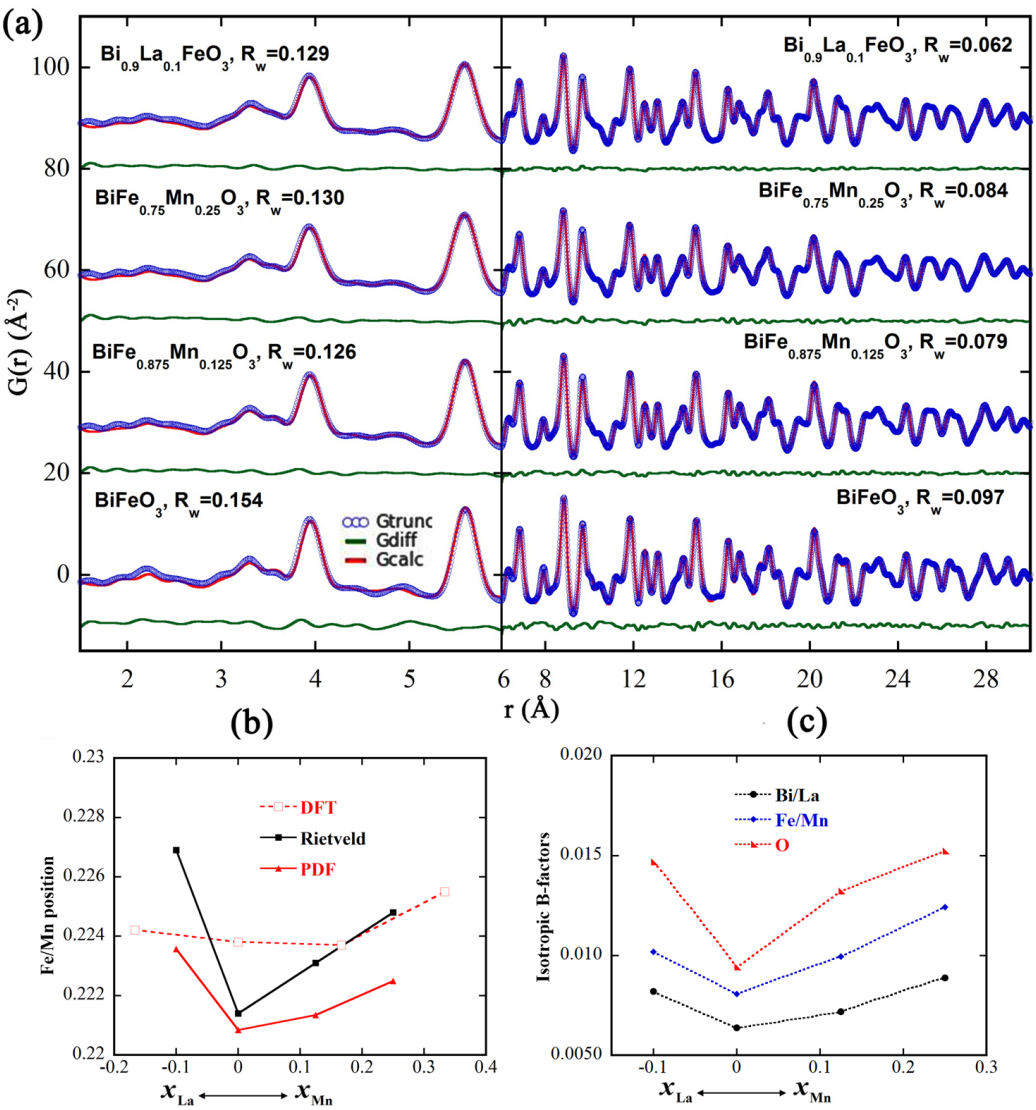

Fig. 4. (a) Experimental Pair Distribution Functions (PDF) G(r) over low and high r regions in pure $BiFeO_3$ and Mn/La doped $BiFeO_3$ fitted to the *R*3*c* structure. Open circles: experimental data; red solid lines: calculated data; the green difference curves shown below each plot. (b) Fe/Mn position from PDF average range (triangle symbols with solid lines) compared with DFT calculated (open symbols with dashed lines) and experiment (filled symbols with solid lines). (c) Debye-Waller factors from PDF refinement over a 30 Å range as a function of chemical composition.

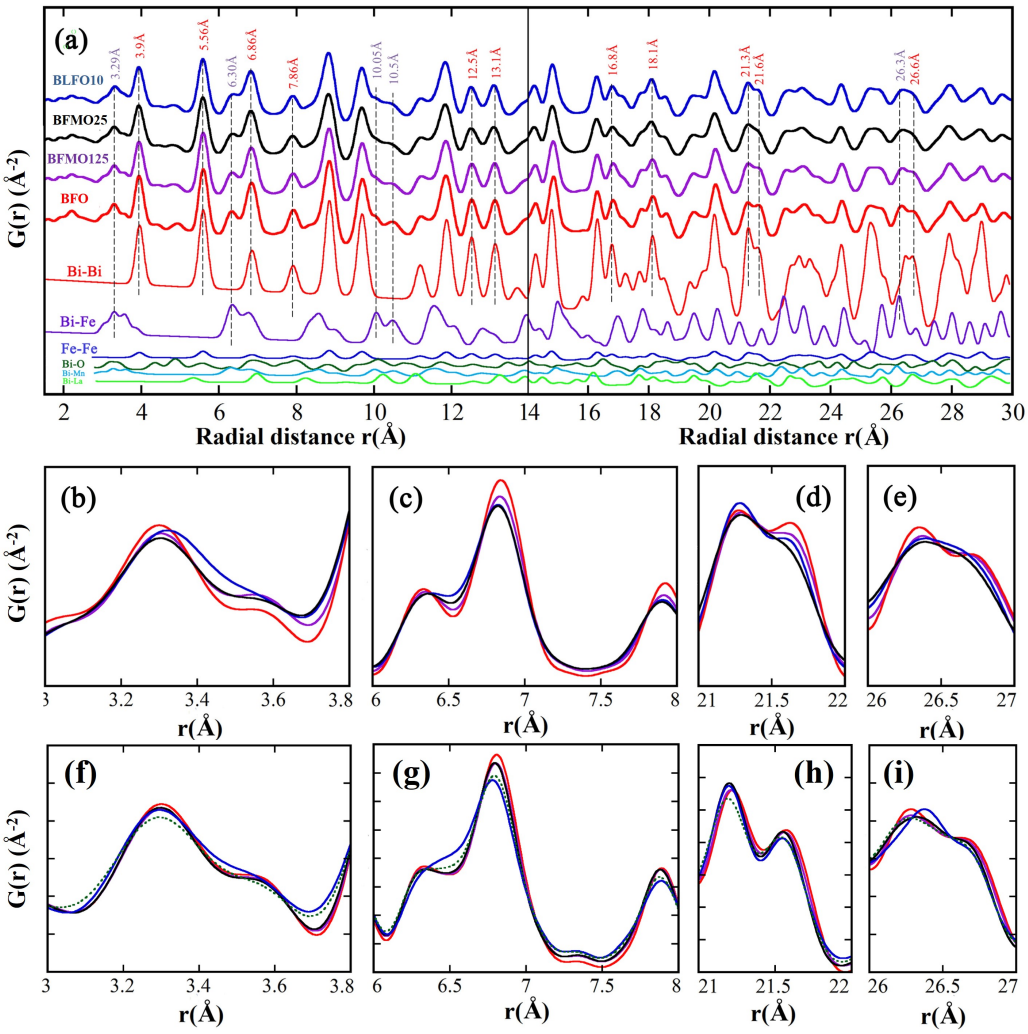

Fig. 5. (a) is the experimental and simulated partial PDFs computed from the hexagonal *R*3*c*-type structure. BFMO125, BFMO25, and BLFO10 mean $BiFe_{0.875}Mn_{0.125}O_3$, $BiFe_{0.75}Mn_{0.25}O_3$ and $Bi_{0.9}La_{0.1}FeO_3$ separately. The PDF patterns are off-set for clarity. (b), (c), (d) and (e) zoom in on selected PDF peaks, with colors corresponding to the legend in panel (a). Panels (f-i) are PDFs simulated from the DFT relaxed structures in Table 3, with the exception of $Bi_4La_2Fe_6O_{18}$. In (f-i) the red, purple, black and blue solid lines correspond to $Bi_6Fe_6O_{18}$, $Bi_6Fe_5MnO_{18}$, $Bi_6Fe_4Mn_2O_{18}$ and $Bi_5LaFe_6O_{18}$, respectively, while the green dashed line corresponds to $Bi_{23}Fe_{21}Mn_3O_{72}$.

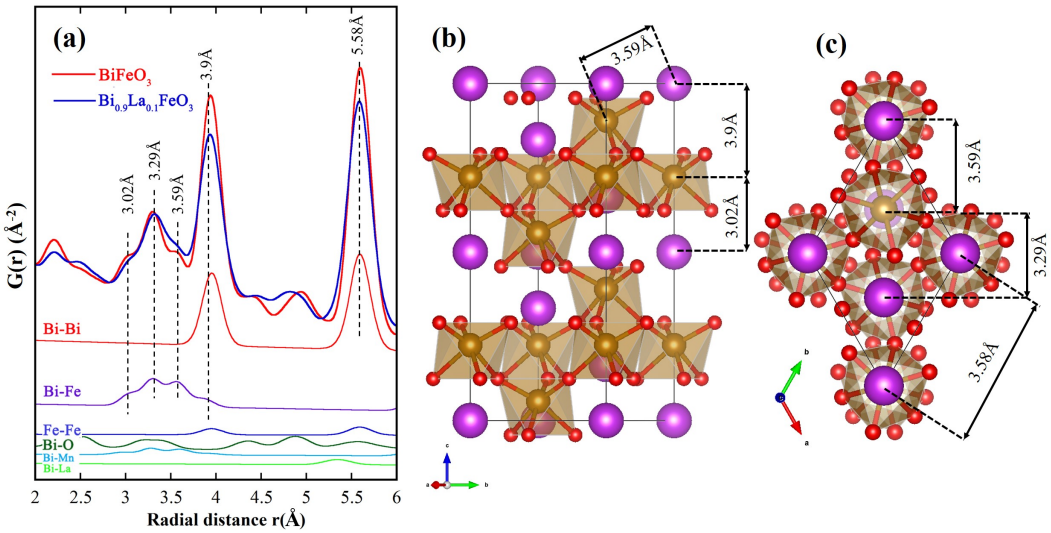

Fig. 6. (a) comparison of low-r part of the La-doping $BiFeO_3$, pure $BiFeO_3$ and simulated partial PDFs computed from the *R*3*c* -type structure, (b) and (c) are the fragment of Bi involving interatomic distance along the different direction of hexagonal unit cell of *R*3*c*.

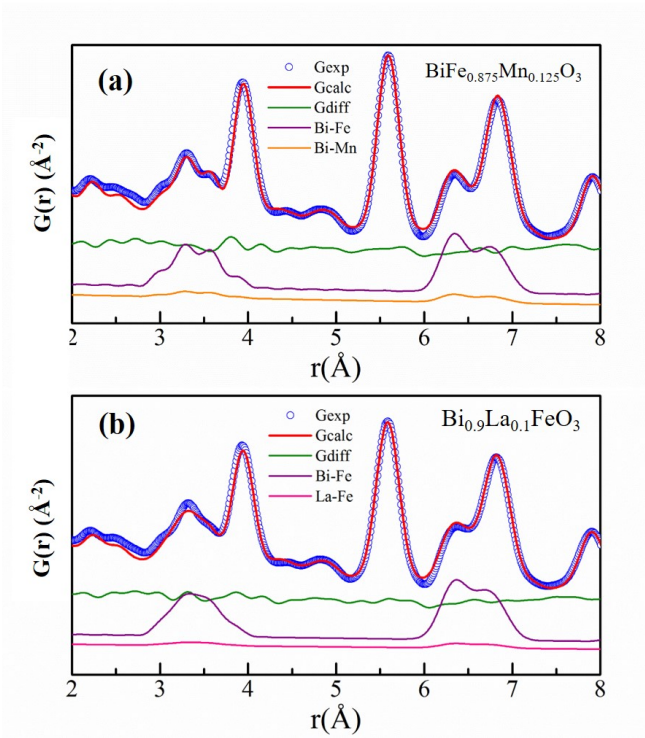

Fig. 7. Low-r part of the experimental PDFs of (a) $BiFe_{0.875}Mn_{0.125}O_3$ and (b) $Bi_{0.9}La_{0.1}FeO_3$ with corresponding simulated partial PDFs.

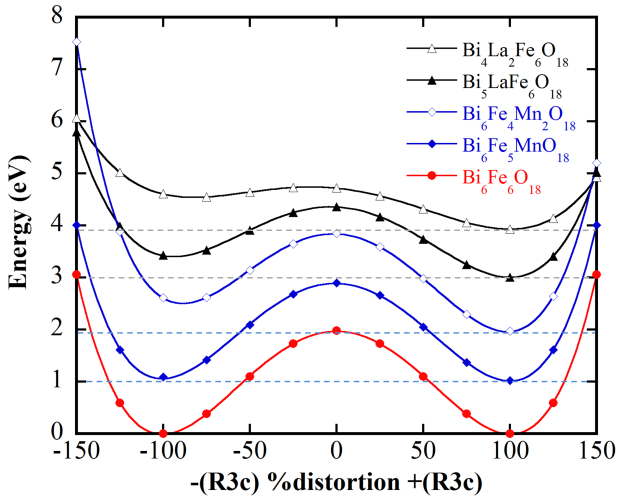

Fig. 8. Ferroelectric double-wells in the form of the calculated total energy upon displacements along the polar [001] direction in the *R*3*c* hexagonal structure for the pure and doped $BiFeO_3$. The curves are displaced along the y-axis for readability.

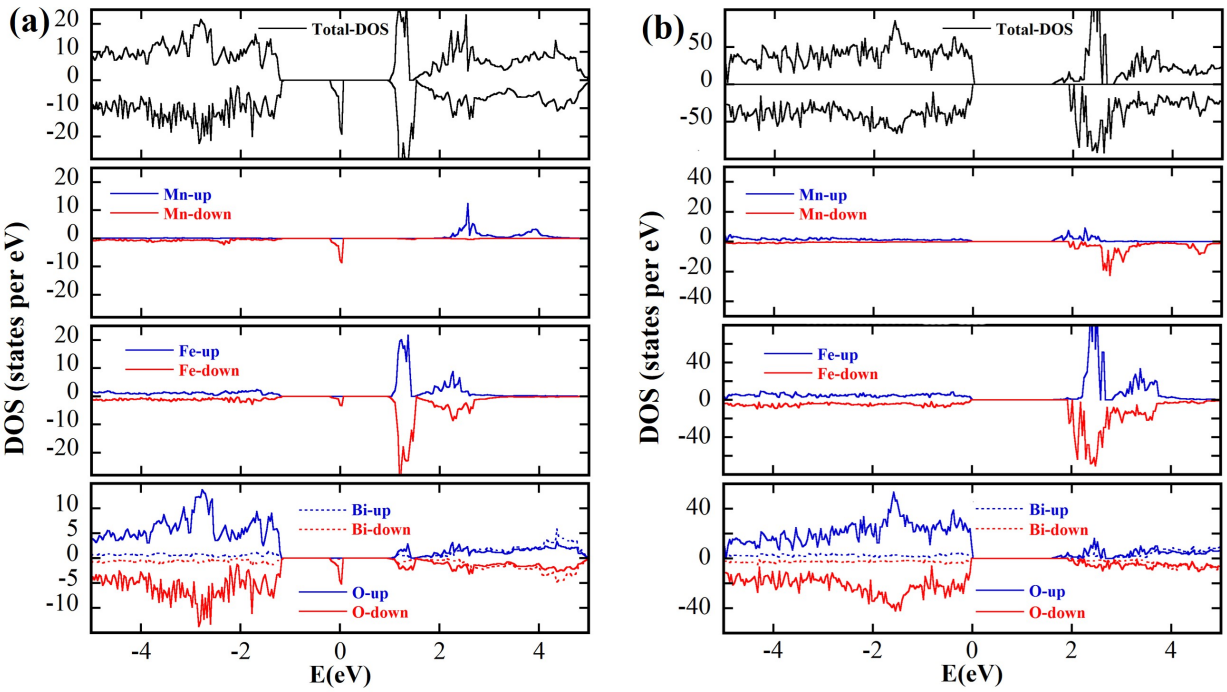

Fig. 9. Total and partial electronic density of states (DOS) of (a) $Bi_6Fe_5MnO_{18}$ and (b) $Bi_{23}Fe_{21}Mn_3O_{72}$.